Article

Not peer-reviewed version

Lightweight and Energy-Efficient Object Localization in Electrical Impedance Tomography via Task-Oriented Inference

Reiji Kaneko and Takashi Ikuno *

Posted Date: 27 January 2026

doi: 10.20944/preprints202601.2062.v1

Keywords: electrical impedance tomography; object localization; task-oriented inference

Article

Lightweight and Energy-Efficient Object Localization in Electrical Impedance Tomography via Task-Oriented Inference

Reiji Kaneko and Takashi Ikuno *

Tokyo University of Science, Japan

* Correspondence: tikuno@rs.tus.ac.jp

Abstract

We propose a lightweight, task-oriented inference framework for object localization in electrical impedance tomography (EIT) without solving the inverse reconstruction problem. Training data were generated by finite element method (FEM) simulations for Opposite and Adjacent current injection configurations. A simple feedforward neural network independently estimated radial and angular object positions as probability distributions. These distributions were visualized and quantitatively evaluated using the Wasserstein distance. Results show that the Opposite configuration produces more localized, unimodal probability distributions than the Adjacent configuration by alleviating informational ambiguity in the central region. Experimental EIT measurements confirmed robustness, and the proposed approach significantly reduced energy consumption from 3.09 Wh to 0.96 Wh, demonstrating over three times higher efficiency than conventional methods. This task-oriented framework enables reliable and energy-efficient localization for low-power EIT applications.

Keywords: electrical impedance tomography; object localization; task-oriented inference

1. Introduction

Electrical impedance tomography (EIT) has been widely studied as a non-invasive imaging technique, in which the primary objective is to reconstruct the spatial conductivity distribution by solving an ill-posed inverse problem.[1] Owing to its safety and versatility, EIT has attracted considerable attention in medical, industrial, and environmental sensing applications.[2–8] In many practical scenarios, however, EIT is expected to operate under strict constraints on computational resources and power consumption, such as mobile, portable, or battery-powered sensing systems.[9–11] In these contexts, the computational burden associated with inverse-problem-based image reconstruction becomes a critical limitation.

Moreover, in a wide range of real-world applications, full conductivity reconstruction is not always required. Instead, only coarse but task-relevant information, such as the presence and approximate location of an object, may be sufficient to achieve the intended sensing objective. Examples include bedside or home healthcare monitoring, on-site infrastructure inspection, and continuously deployed environmental or agricultural sensors.[12–17] In particular, object localization represents one of the most fundamental and practically useful tasks in EIT-based sensing.

Conventional reconstruction-based approaches inherently rely on iterative solvers and large-scale numerical computations, which lead to substantial energy consumption even when the final task requires only limited spatial information. This mismatch between the computational cost and the required information poses a fundamental challenge for practical and energy-efficient EIT deployment.[18–20]

In this study, we propose a lightweight, task-oriented inference framework that directly estimates the object location from EIT boundary voltage measurements without solving the inverse

 doi:10.20944/preprints202601.2062.v1

problem. By focusing on the essential task information rather than full image reconstruction, the proposed approach enables energy-efficient EIT operation and is particularly suited for mobile and resource-constrained sensing applications.

The transition from conventional full image reconstruction to the proposed task-oriented inference necessitates a strategic selection of the physical sensing modality. For the neural network to accurately estimate the object location, the presence of the object must significantly perturb the injected current, manifesting as detectable variations in the boundary potential. Consequently, the robustness of the inference is dictated by the homogeneity of the sensitivity distribution. The excitation strategy must ensure that the object's presence at any coordinate including the central region induces a sufficiently detectable signal response.

To investigate the optimal conditions for achieving this required sensitivity, we focus on the strategy of current excitation. In EIT, the spatial distribution of the sensing field is primarily determined by the electrode configuration used for current injection. We comparatively evaluated two representative strategies: the Adjacent method, where current is injected through neighboring electrodes [15,16], and the Opposite method, where current is injected through electrodes positioned 180° apart. We hypothesize that the Opposite configuration, by forcing current streamlines to traverse the entire domain, provides a more uniform signal response across the specimen than the Adjacent method. This enhanced homogeneity is expected to alleviate the informational bottleneck for central object localization, enabling the lightweight neural network to extract critical features more effectively from a lower-dimensional input space. In this study, we empirically validate this hypothesis by evaluating the localization performance and energy efficiency of both excitation strategies.

2. Materials and Methods

2.1. FEM-Based Forward Simulation and Dataset Generation

In this study, we aim to develop a lightweight machine learning model that can estimate object locations with low computational cost without performing inverse-problem-based image reconstruction. To systematically generate training datasets for this purpose, numerical simulations based on the finite element method (FEM) were conducted for two current injection and voltage measurement configurations in EIT measurements, namely the Opposite and Adjacent methods[19].

Numerical simulations were performed using COMSOL Multiphysics 6.2 with a two-dimensional circular domain of 100 mm in diameter. Eight electrodes were equally spaced along the boundary, and contact impedance was neglected, as shown in Figure 1(a). Direct current (DC) was injected with a current density of 100 A/m^2. The mesh consisted of free triangular elements and was locally refined near the electrodes and the object to ensure numerical accuracy.

The background conductivity was set to 0.1 S/m, and a single circular object with a conductivity of 10^7 S/m was embedded in the domain. The object diameter was varied from 1 to 49 mm. The object location was defined in polar coordinates (r, θ), where r was discretized into 11 levels from 1 to 41 mm and θ ranged from 0° to 352.5° in 7.5° increments. These discretized values of r and θ were used as class labels in the machine learning model.

In the Opposite method, current was injected between diametrically opposite electrodes, and voltage differences were measured across three electrode pairs perpendicular to the injection axis. The injection electrodes were sequentially switched to form eight injection patterns (I–V, II–VI, …, VIII–IV), yielding three voltage differences per injection and a total of 24 measurements.

In the Adjacent method, current was injected between neighboring electrodes, and voltage differences were measured across five adjacent electrode pairs, excluding the injection electrodes. The injection pattern was sequentially rotated to form eight configurations, yielding five voltage differences per injection and a total of 40 measurements.

We developed a lightweight machine learning model that directly estimates the object center from boundary voltage measurements without solving the EIT inverse problem, enabling low

 doi:10.20944/preprints202601.2062.v1

computational cost and power consumption by inferring class probabilities without image reconstruction.

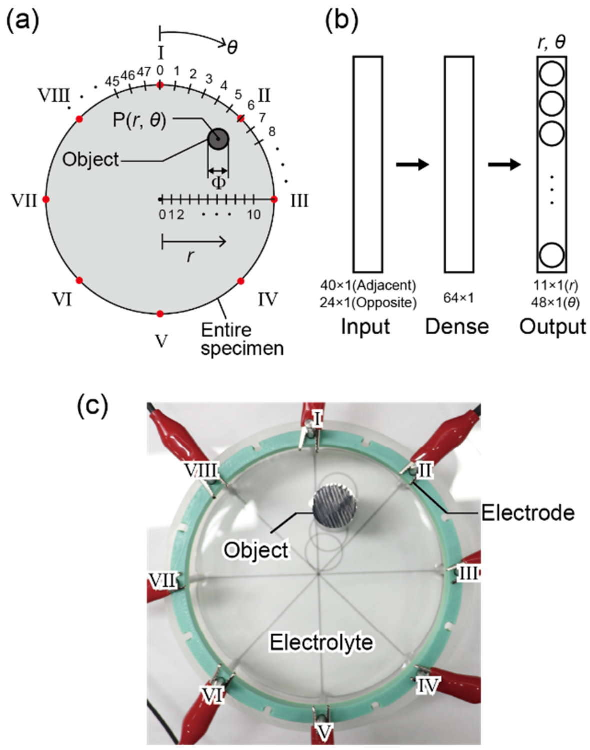

Figure 1. (a) Definition of the object location using polar coordinates (r, θ) in a circular specimen equipped with eight electrodes. (b) Schematic diagram of the lightweight machine learning model. (c) Photograph of the experimental setup.

2.2. Lightweight Inference Model

Figure 1(b) illustrates the structure of the object localization algorithm based on a neural network that takes voltage difference data as input. The model consists of an input layer, a single fully connected layer, and an output layer. The rectified linear unit (ReLU) function was used as the activation function for the fully connected layer, while the Softmax function was applied to the output layer. The loss function was defined as the categorical cross entropy loss. The number of training epochs and the batch size were set to 50 and 32, respectively. The machine learning model was implemented using TensorFlow 2 with Python 3.10.

A total of 5,136 datasets were generated by FEM-based forward simulations, of which 5,084 were used for training and 52 for testing. Each dataset assumed a single object characterized by three parameters: the object diameter Φ, the radial distance r, and the rotation angle θ.

The normalized voltage difference data were used as inputs, and two separate models were trained to estimate the radial distance r and the rotation angle θ. The r-estimation model outputs an 11-class probability distribution corresponding to 1 mm [0], 5 mm [1], …, and 41 mm [10], while the θ-estimation model outputs a 48-class probability distribution corresponding to 0° [0], 7.5° [1], …, and 352.5° [47]. Separate models were trained using voltage difference data from the Opposite and Adjacent methods, and their object localization performance was quantitatively compared.

2.3. Experimental Validation

To validate the proposed method, solution-based EIT experiments were conducted. Figure 1(c) shows the experimental setup and electrode configuration. A cylindrical container (100 mm in diameter) was filled with a 0.1 mol/L sodium hydroxide solution (conductivity: 2.18 S/m), and a single SUS304 cylindrical object (15 mm in diameter) was placed in the solution.

 doi:10.20944/preprints202601.2062.v1

The object location was defined in polar coordinates (r, θ), and measurements were performed for selected values of r and θ. Experiments were conducted at r = 9, 17, 25, and 33 mm and θ = 0°, 7.5°, and 15°, corresponding to a subset of the simulated positions. Eight stainless steel electrodes (SUS303, 3 mm in diameter) were uniformly arranged inside the container.

A DC/AC current and voltage source (155-AC, Lake Shore Cryotronics Inc., USA) was used for current injection, and voltage measurements were performed using a digital multimeter (GDM-8261A, TEXIO TECHNOLOGY CORPORATION, Japan). The measurements were carried out with an injection current of 5 mA and a measurement frequency of 1 kHz.

To quantitatively evaluate the discrepancy between the estimated object location probability distributions and the ideal probability distribution, the Wasserstein distance was employed as an evaluation metric. A two-dimensional probability distribution of the object location, denoted as $P(r,\theta)$, was constructed as follows.

$$P(r,\theta) = \frac{P(r)P(\theta)}{\sum_{r,\theta} P(r)P(\theta)}$$

Here, $P(r)$ represents the probability of the object being present at the radial distance r, and $P(\theta)$ represents the probability of the object being present at the rotation angle θ. The Wasserstein distance $w_1(P,Q)$ is defined by the following equation.[21]

$$w_1(P,Q) = \sum_{r,\theta} P(r,\theta)\|(r,\theta) - (r_0,\theta_0)\|$$

Here, (r_0,θ_0) denotes the object location corresponding to the ground-truth label. A smaller Wasserstein distance indicates that the estimated probability distribution is more localized around the true object position.

3. Results and Discussion

3.1. Analysis of Marginal Probability Distributions

Figure 2(a) presents the marginal probability distributions of the estimated object location, $P(r)$ and $P(\theta)$, for an object fixed at (r, θ) = (6, 2). These results reveal how the physical current excitation strategy fundamentally shapes the neural network's ability to resolve spatial coordinates.

In the Opposite method, $P(r)$ exhibits a sharp, unimodal peak at r = 5, aligning closely with the ground truth. This indicates that the penetrating current field provides a distinct voltage signature for different radial positions, even near the center. In contrast, the Adjacent method displays a bimodal distribution, with peaks split between r = 3 and r = 8. This "splitting" of probability suggests a radial ambiguity; the localized sensitivity of the adjacent configuration makes it difficult for the model to distinguish whether the object is closer to the center or the periphery, as both positions may induce similar perturbations in the boundary potential.

A similar trend is observed in the angular distribution $P(\theta)$. The Opposite method yields a concentrated peak at θ = 2, demonstrating high angular discriminability. This is because the diametrical current injection axis creates a global potential gradient that is highly sensitive to the object's rotation. While the Adjacent method manages to form a peak at θ = 1, the distribution is noticeably broader and less certain. This "blurred" angular response is a direct consequence of the sensing field being confined to the region near the electrodes, which limits the model's ability to pinpoint the exact angular coordinate of a central object.

 doi:10.20944/preprints202601.2062.v1

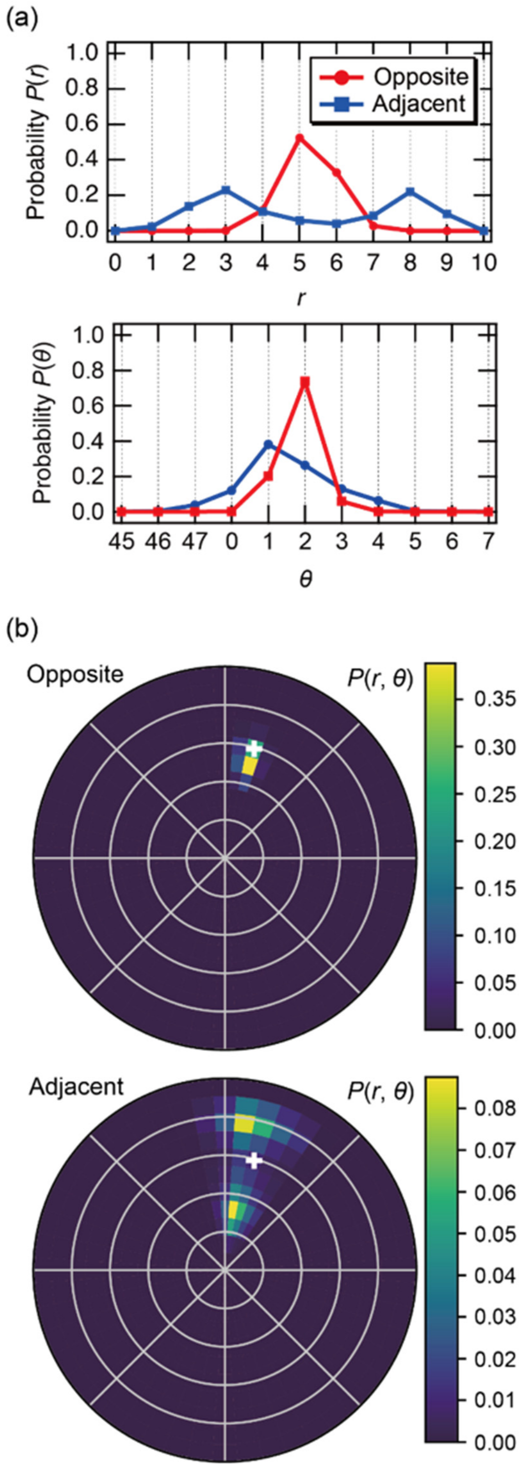

Figure 2. (a) Marginal probability distributions of the object location: radial distribution $P(r)$ and angular distribution $P(\theta)$, obtained from measurement data in which the object position (r, θ) was (6, 2). (b) Schematic visualization of the spatial probability distribution $P(r, \theta)$ in the (r, θ) space. The plus symbol indicates the actual object position.

3.2. *Visualization of Localization Certainty via 2D Probability Mapping*

Figure 2(b) displays the two-dimensional probability distributions $P(r, \theta)$ reconstructed from the independent radial and angular estimations. This mapping serves as a direct visualization of the model's spatial "confidence" in pinpointing the object center.

In the Opposite method, the probability mass is highly concentrated into a single, well-defined region that accurately encompasses the actual object position. The absence of peripheral "noise" or

 doi:10.20944/preprints202601.2062.v1

secondary peaks in the 2D plane demonstrates that the features extracted from the penetrating current field are spatially unique. This confirms that the Opposite configuration effectively eliminates the ambiguity in the mapping between boundary voltages and coordinates, providing a reliable foundation for lightweight task-oriented inference.

Conversely, the Adjacent method exhibits a significant "ghosting" effect, where high-probability regions are scattered across two disparate locations. This spatial fragmentation is the 2D manifestation of the bimodal distribution observed in $P(r)$ in Figure 2(a). Because the sensitivity of the adjacent field decays rapidly toward the center, the neural network encounters an informational symmetry where different (r, θ) coordinates produce nearly identical voltage perturbations. Consequently, the model cannot converge on a unique solution, resulting in a "blurred" and unreliable localization. This result highlights that without a physics-optimized sensing strategy, even a neural network trained on extensive datasets cannot overcome the inherent physical limitations of the sensing modality.

3.3. Quantitative Evaluation of Localization Error

Figure 3 presents the Wasserstein distances of the object location probability distributions $P(r, \theta)$ obtained from experimental data. A comparison between the Adjacent and Opposite methods shows that, except for the case of $(r, \theta) = (2, 0)$, the Opposite method yields smaller Wasserstein distances for all object locations.

These results indicate that the probability distributions estimated by the Opposite method are more strongly concentrated around the ground-truth labels than those obtained by the Adjacent method. In other words, the Opposite method exhibits lower ambiguity in object localization and enables more unique and reliable position estimation.

From these results, it is evident that differences in current injection and voltage measurement configurations have a significant impact on object localization performance. The higher positional discriminability observed with the Opposite method is attributed to the fact that the current injection axis traverses the entire domain, thereby enhancing both the angular dependence of the voltage distribution and the sensitivity to deeper regions of the medium. As a result, the amount of informative content contained in the boundary voltage differences increases, and features related to the object location become more pronounced.

In contrast, in the Adjacent method, the injected current predominantly flows in the vicinity of the electrodes, leading to a relatively localized sensitivity distribution within the domain. This reduces discriminability in both the angular and radial directions. Consequently, the probability distributions estimated by the machine learning model become more spread out, resulting in increased uncertainty in object localization.

Notably, although the Adjacent method has a higher input dimensionality (40 dimensions) than the Opposite method, it does not necessarily achieve superior estimation accuracy. This result suggests that object localization performance is governed not by the number of input features itself, but by the structure of the physical sensitivity distribution inherent in the current injection and measurement configuration.

In addition, the two-dimensional probability distributions shown in Figure 2(b) do not represent reconstructed conductivity images, but rather directly visualize the existence probability of the object center. This representation demonstrates that the positional information embedded in EIT measurement data can be quantitatively and intuitively evaluated without solving the inverse problem.

Preprints.org (www.preprints.org) | NOT PEER-REVIEWED | Posted: 27 January 2026 doi:10.20944/preprints202601.2062.v1

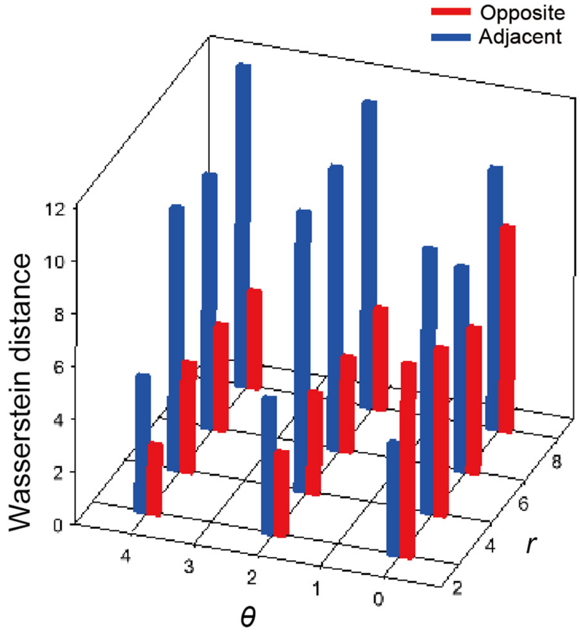

Figure 3. Wasserstein distance as a function of r and θ.

3.4. Computational Cost and Energy Consumption

To evaluate the computational cost of object localization, energy consumption on a PC was compared between a conventional inverse-problem-based reconstruction method using EIDORS[1)] and the proposed lightweight machine learning approach under the same computational environment. The EIDORS-based method consumed 3.09 Wh, whereas the proposed approach consumed 0.96 Wh for the Opposite method and 0.94 Wh for the Adjacent method.

These results confirm that the proposed method achieves a substantial reduction in energy consumption compared with conventional reconstruction-based approaches. This improvement demonstrates the high computational efficiency of the proposed framework, which directly estimates object locations from low-dimensional feature representations without performing image reconstruction.

4. Conclusions

In this study, we proposed a lightweight machine learning approach for directly estimating object center positions from EIT boundary voltage measurements without inverse-problem-based image reconstruction. Using FEM-generated datasets, object localization performance was systematically compared between the Opposite and Adjacent current injection methods.

The results show that the Opposite method yields more spatially localized object location probability distributions and smaller Wasserstein distances than the Adjacent method, as confirmed by both visualization and quantitative evaluation. Experimental measurements further demonstrated a significant reduction in energy consumption compared with conventional inverse-problem-based reconstruction methods.

The proposed method does not aim to reconstruct detailed conductivity distributions; instead, it represents a task-oriented EIT inference framework that directly maps boundary voltage measurements to the object location of interest. This approach enables sufficient localization accuracy for practical applications while effectively reducing computational cost and energy consumption.

The framework presented in this study is well suited for EIT applications in resource- and power-constrained environments, such as mobile sensing and embedded systems, and is expected to facilitate the development of future low-power EIT-based sensor systems.

Author Contributions: Conceptualization, T.I; methodology, T.I; software, R.K. and T.I.; validation, T.I.; formal analysis, T.I. and R.K.; investigation, R.K.; resources, T.I.; data curation, R.K.; writing—original draft preparation, R.K.; writing—review and editing, T.I.; visualization, T.I. and R.K.; supervision, T.I.; project administration, T.I.; funding acquisition, T.I. All authors have read and agreed to the published version of the manuscript.

Funding: This research was funded by Kajima Foundation and the Top Researcher Development Program of Tokyo University of Science.

Informed Consent Statement: Not applicable.

Data Availability Statement: The data presented in this study are available on request from the corresponding author.

Acknowledgments: This work was partly supported by Kajima Foundation and the Top Researcher Development Program of Tokyo University of Science.

Conflicts of Interest: The authors declare no conflicts of interest. The funders had no role in the design of the study; in the collection, analyses, or interpretation of data; in the writing of the manuscript; or in the decision to publish the results.

References

1. Adler, A.; Lionheart, W.R.B. Uses and abuses of EIT: A critical review. *Physiol. Meas.* **2006**, *27*, S25.
2. Adler, A.; Grychtol, B.; Bayford, R. Developments in electrical impedance tomography (EIT) for lung monitoring. *Physiol. Meas.* **2015**, *36*, 1067.
3. Wu, C.; Soleimani, M. Adaptive and focused electrical impedance tomography. *IEEE Access* **2019**, *7*, 21870–21882.
4. Xie, Y.; Liu, F.; Sun, J.; Suo, P.; Xu, L.; Du, K.; Xu, H.; Feng, J.; Liang, H. Intelligent electrical impedance tomography for object localization using deep learning. *IEEE Trans. Instrum. Meas.* **2024**, *73*, 1–12.
5. Krol, K.; Klosowski, G.; Rymarczyk, T.; Gauda, K.; Kulisz, M.; Golec, E.; Surowiec, A. Energy-efficient EIT image reconstruction for portable systems. *Energies* **2025**, *18*, 5956.
6. Kulisz, M.; G. Klosowski; T. Rymarczyk; J. Sloniec; K. Gauda; W. Cwynar. Low-power consumption in electrical impedance tomography systems. *Energies* **2024**, *17*, 681.
7. Zhao, P.F.; Fan, L.F.; Wang, Y.Q.; Li, Y.; Wang, N.; Cheng, Q.; Wang, Z.Y.; Huang, L. A fast and robust image reconstruction algorithm for EIT. *Measurement* **2022**, *192*, 110874.
8. Kawashima, D.; Yuki, T.; Li, S.S.; Takei, M. High-speed electrical impedance tomography for cellular imaging. *Biosens. Bioelectron.* **2022**, *212*, 114432.
9. Pennati, F.; Angelucci, L.; Morelli, L.; Bardini, S.; Barzanti, E.; Cavallini, F.; Conelli, A.; Federico, G.D.; Paganelli, C.; Aliverti, A. Wearable EIT systems for respiratory monitoring: A review of current technologies and challenges. *Sensors* **2023**, *23*, 1182.
10. Zamora-Arellano, F.; Lopez-Bonilla, O.R.; Garcia-Guerrero, E.E.; Olguín-Tiznado, J.E.; Inzunza-Gonzalez, E.; Lopez-Mancilla, D.; Tlelo-Cuautle, E. Deep learning-based reconstruction for EIT using specialized hardware. *Electronics* **2021**, *10*, 15.
11. Li, D.M.; Wang, L. Real-time object identification in EIT via deep neural networks. *IEEE Trans. Instrum. Meas.* **2024**, *73*, 1–10.
12. Xu, C.; Dai, M.; You, F.; Shi, X.; Fu, F.; Liu, R.; Dong, X. An optimized EIT system for bedside lung monitoring. *Physiol. Meas.* **2011**, *32*, 585.
13. Yu, H.; Dong, Z.X.; Han, W.; Wu, Y.; Wang, C.P.; Liu, Z.; Jia, J.B. Evaluation of medical EIT systems for clinical diagnostics. *Measurement* **2025**, *256*, 117986.

 doi:10.20944/preprints202601.2062.v1

14. Jeon, D.; Kim, M.K.; Jeong, Y.; Oh, J.E.; Moon, J.; Kim, D.J.; Yoon, S. Automated inspection of industrial structures using EIT. *Autom. Constr.* **2022**, *135*, 104116.
15. Minakawa, K.; Ohta, K.; Komatsu, H.; Fukuyama, T.; Ikuno, T. Flexible electrode array for optimized EIT measurement. *AIP Adv.* **2024**, *14*, 015210.
16. Kaneko, R.; Minakawa, K.; Ikuno, T. Lightweight inference for object localization in EIT. *J. Jpn. Soc. Appl. Electromagn. Mech.* **2025**, *33*, 300–306 (in Japanese).
17. Yu, H.; Liu, Z.; Song, M.; Liu, L.; Liu, Z.; Cao, E.; Zhao, X. Environmental impact of industrial waste detection using EIT. *Environ. Pollut.* **2025**, *372*, 126032.
18. Neumayer, M.; Suppan, T.; Bretterklieber, H.; Wegleiter, H.; Fox, C. Assessing accuracy of EIT using Wasserstein metrics. *Mathematics* **2024**, *12*, 1023.
19. Khan, T.A.; Ling, S.H. Machine learning algorithms for improved EIT localization. *Algorithms* **2019**, *12*, 88.
20. Coxson, A.; Mihov, I.; Wang, Z.; Avramov, V.; Barnes, F.B.; Slizovskiy, S.; Mullan, C.; Timokhin, I.; Sanderson, D.; Kretinin, A.; et al. Nanoscale EIT and inverse problems. *Inverse Probl.* **2022**, *38*, 085007.
21. Zhu, Z.; Wang, L.; Peng, G.; Li, S. Deep learning based EIT reconstruction for industrial applications. *Sensors* **2021**, *21*, 4394.